Characterizing Adhesion between a Micro-Patterned Surface and a Soft Synthetic Tissue

Journal:	*Langmuir*
Manuscript ID	la-2016-03643d.R2
Manuscript Type:	Article
Date Submitted by the Author:	n/a
Complete List of Authors:	Kern, Madalyn; University of Colorado Boulder, Mechanical Engineering Qi, Yuan; University of Colorado Boulder, Mechanical Engineering Long, Rong; Univ. of Colorado Boulder, Mechanical Engineering Rentschler, Mark; University of Colorado Boulder, Mechanical Engineering

Characterizing Adhesion between a Micro-Patterned Surface and a Soft Synthetic Tissue

Madalyn D. Kern, Yuan Qi, Rong Long, and Mark E. Rentschler*

Department of Mechanical Engineering, University of Colorado, Boulder

E-mail: mark.rentschler@colorado.edu

Abstract

Work of adhesion and work of separation are characteristic properties of a contact interface which describe the amount of energy per unit area required to adhere or separate two contacting substrates, respectively. In this work, the authors present experimental and data analysis procedures which allow the contact interface between a soft synthetic tissue and a smooth or micro-patterned polydimethylsiloxane (PDMS) substrate to be characterized in terms of these characteristic parameters. Due to physical geometry limitations, the experimental contact geometry chosen for this study differs from conventional test geometries. Therefore, the authors used finite element modeling to develop correction factors specific to the experimental contact geometry used in this work. A work of adhesion was directly extracted from experimental data while the work of separation was estimated based on experimental results. These values are compared to other theoretical calculations for validation. The results of this work indicate that the micro-patterned PDMS substrate significantly decreases both the work of adhesion and work of separation as compared to a smooth PDMS substrate when in contact with a soft synthetic tissue substrate.

1 Introduction

Adhesion is a complex phenomenon which continues to intrigue researchers and practitioners across many disciplines. As two surfaces approach and contact each other, an attractive force between the surfaces may be present, causing the surfaces to stick together and resist tensile loading. Several contact mechanics theories, dating back to the early 1970's, have been established to describe this adhesive response.[1–5] Of these theories, the Johnson-Kendall-Roberts (JKR) contact theory[2] is frequently used to interpret indentation experiments and to extract work of adhesion and work of separation, characteristic parameters of adhesion which are independent of contact geometry.[6]

More recently, robotic locomotion has given rise to a large body of adhesion literature where researchers have investigated the effect of adding surface patterns to a compliant surface to enhance adhesion when contacting a smooth, rigid surface.[7–16] The addition of surface patterns was motivated by the natural ability of geckos and some insects to climb vertical and overhung walls, a behavior which has been attributed to the fibrillar structure on these animals' foot pads.[17,18] In this body of literature, the diameter of the fibrils often spans both the nanometer and micrometer length scales and the fibril aspect ratio (height:diameter) is typically much greater than one.[14,19] The physical mechanism for the enhanced adhesion is thought to be multi-faceted including effects from contact splitting,[9,14,19] flaw insensitivity,[8,10,20] and energy dissipation through dynamic instability.[21,22]

On the other hand, the contact interface between a rigid, rough surface and a smooth, compliant substrate has been shown to decrease the adhesive response and is attributed to the decrease in actual contact area as a result of the surface roughness.[3,23] However, it is also understood that if the compliant material is soft enough and the surface roughness shallow enough, adhesion can actually be increased due to the penetration of the compliant material into the rough surface profile, thus, increasing the contact area.[24,25] Empirical models have been developed to predict the actual contact area as a function of normal applied load and surface roughness geometry, although the experimental work done in this area has been with two substrates of comparable modulus or where the roughness is modeled by sinusoidal waves along the surface.[26,27]

Clearly, the body of literature demonstrates that an adhesive response can be tuned to achieve specific outcomes, allowing practitioners to optimize the behaviors of certain interfaces. One area of the authors' previous research has been in the design and development of a Robotic Capsule Endoscope (RCE), a surgical device capable of traveling through the gastro-intestinal (GI) tract for diagnostic and therapeutic purposes.[28,29] For this specific application, the authors are interested in optimizing the mobility of the RCE by maximizing the tractive response while minimizing the adhesive response generated by the RCE's mobility mechanism. Several different mobility mechanisms have been pursued for RCE's including inchworm mobility,[30] legged mobility,[31] magnetic mobility[32] and, as in the authors' case, wheeled mobility.[28,29] The authors' wheeled mobility approach uses multiple tank-like polydimethylsiloxane (PDMS) wheels with a micro-patterned surface to drive the robotic unit through the GI tract.[29] The translational, tractive, response of the micro-structure against a soft biological tissue has been studied previously and design optimization relationships have been presented.[33–35] While some normal adhesion characterization work has been completed,[31,36,37] an experimental platform which characterizes the work of adhesion and work of separation between the micro-patterned surface and a soft, tissue-like, substrate has not yet been presented. Both the work of adhesion and work of separation are material surface properties insensitive to experimental geometry and thus, valuable parameters which can be compared across experimental tests.

In this work, the authors present two main contributions: (1) experimental and data analysis procedures for characterizing the adhesion energy between a smooth or micro-patterned PDMS substrate and a soft synthetic tissue and (2) discussion of the effect on normal adhesion when a cylindrical pillar micro-pattern is added to a PDMS surface in contact with a soft synthetic tissue - an experimental configuration which has not yet been explicitly tested. In Section 2 the authors describe the experimental methods used for material and adhesion characterization and detail the computational methods used to define correction factors to account for the unique experimental contact geometry. The experimental results from material characterization, correction factor validation and adhesion characterization are presented and discussed in Section 3. Finally, the conclusions of this work are presented in Section 4.

2 Experimental

The conventional experimental indentation geometry used to support Hertz and JKR contact theories are illustrated in Figure 1. Both the Hertz and JKR theories are based on the assumption that the elastic substrates are infinitely thick such that they can be treated as an elastic half-space. If, however, substrate thickness is finite, both the Hertz and JKR theories will overestimate the substrate compliance. Thus, correction factors must be applied to account for the finite thickness of the substrate. A complete derivation of these finite thickness correction factors can be found in Kenneth Shull's review paper[6] and are summarized in this paper in Section 2.2.

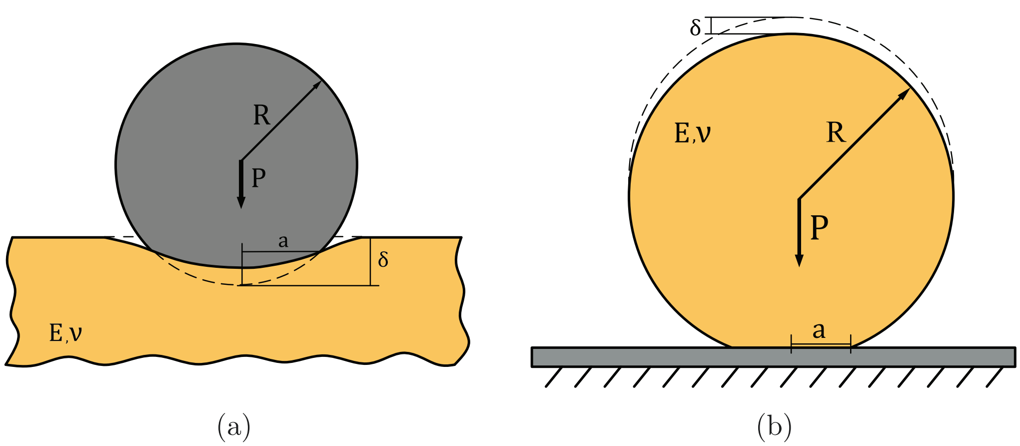

Figure 1: Conventional contact geometries for adhesion testing. Yellow shaded materials represent compliant materials while gray shaded materials represent rigid materials.

Because the authors are ultimately interested in characterizing the adhesive response between a micro-patterned PDMS substrate and a soft synthetic tissue material, the conventional indentation experimental geometries, as shown in Figure 1, present practical limitations. First, the soft synthetic tissue material is not easily grasped without shape deformation when in spherical form. Additionally, since the micro-patterned surface is fabricated on a planar field, wrapping the micro-patterned PDMS substrate around a rigid sphere would result in non-uniform pillar spacing. Therefore, the authors chose to lay the micro-patterned PDMS substrate ($h_{PDMS} = 1\,\text{mm}$) atop a rigid glass plate and use an acrylic sphere ($R = 12.7\,\text{mm}$) wrapped with a thin layer ($h_{syn} = 3\,\text{mm}$) of the synthetic tissue as the contacting probe (Figure 2). Clearly, the experimental contact geometry (Figure 2) is different from conventional contact geometries (Figure 1) and thus, the interpretation of the experimental data will require modifications to the JKR theory.

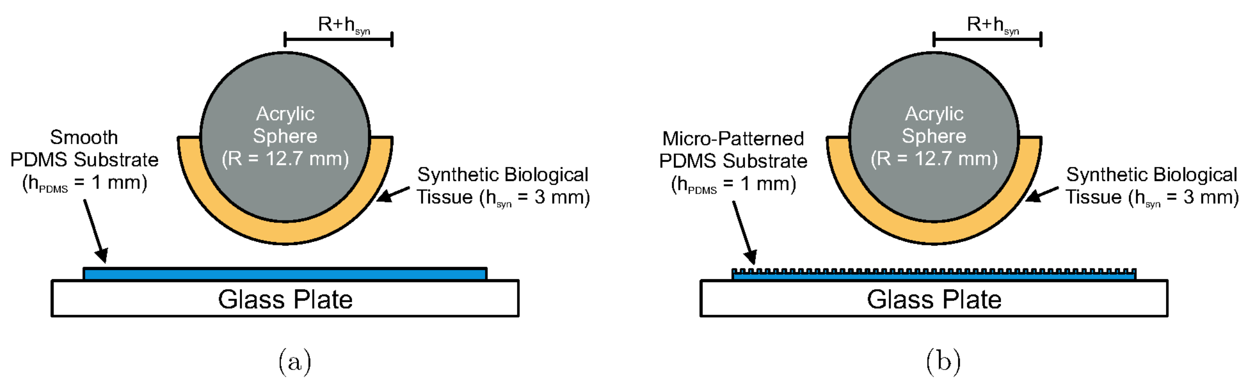

Figure 2: This is a schematic of the experimental geometry used for this work (not drawn to scale). The same spherical probe was used to test both the smooth PDMS (2a) and the micro-patterned PDMS (2b).

The experimental work of this study is organized into three parts: Section 2.1 - material property characterization, Section 2.2 - correction factor determination, and Section 2.3 - adhesion characterization for smooth and micro-patterned surfaces. All experimental work was done using an MTS Insight™ II Material Testing System (MTS Systems Corporation, Eden Prarie, MN) and a 2 N load cell. The contact area at the interface between substrates was measured using an Olympus I-Speed high-speed camera (iX Cameras, Woburn, MA) with a frame rate of 100 fps. Contact area images were post-processed using Matlab R2014b

(Mathworks, Inc., Natick, MA) to identify the contact region and calculate a contact radius (see supporting information document for more details). During experimental testing the spherical probe was lowered at a rate of 0.01 mm/s and retracted at approximately 2 mm/s. The data acquisition rate was set to 100 Hz. While load and displacement data were collected for both the down-stroke (approach) and up-stroke (retraction) test phases, the contact radius data was only collected during the down-stroke test phase. Additional details as to why the authors made this limiting decision can be found in the supporting information for this document. The authors directly extract a work of adhesion from experimental data and estimate the corresponding work of separation. Several test method validation steps were performed before comparing the adhesion response between the synthetic tissue and smooth PDMS or micro-patterned PDMS. Additionally, both the work of adhesion and work of separation values are validated against theoretical bounds.

2.1 Material Property Characterization

The adhesion response of a contact interface is dependent on the elastic modulus and Poisson's ratio of the contacting materials. The authors used Sylgard® 184 Silicone Elastomer (Dow Corning Corporation, Midland, MI) at a 10:1 base:curring agent weight ratio to fabricate the micro-patterned PDMS substrate and a synthetic soft Poly-Vinyl-Chloride (PVC) material (M-F Manufacturing Co, Fort Worth, TX) to fabricate the synthetic tissue substrate. For simplicity, the authors assume that both the PDMS and synthetic tissue materials are incompressible, thus assuming a Poisson's ratio of 0.5. Two different approaches were taken to measure the elastic moduli of the PDMS and synthetic tissue materials.

2.1.1 PDMS Modulus

The elastic modulus of the PDMS material was extracted from an experimental indentation test using a rigid acrylic sphere probe. Load and displacement were measured as the probe approached and contacted a smooth PDMS substrate. An elastic modulus was extracted by comparing the experimental data to Hertz contact theory using a correction factor[6] to account for the finite thickness of the PDMS. Hertz contact theory, rather than JKR contact theory, was used because no measurable adhesion was observed during the down-stroke test phase.

2.1.2 Synthetic Tissue Modulus

The authors chose to extract the elastic modulus for the synthetic tissue substrate using an experimental configuration from which adhesion forces were not observed during the down-stroke test phase. This is because at this point, the work of adhesion and work of separation for the specific contact interface is unknown. As presented and discussed in detail in Section 3.3.1.2, no measureable adhesion forces were observed during the down-stroke test phase of the synthetic tissue probe contacting the micro-patterned PDMS substrate. The experimental data cannot be analyzed using conventional Hertz theory because the experimental contact geometry (Figure 2b) differs from the conventional contact geometries (Figure 1). Therefore, the authors developed a finite element model for the micro-patterned PDMS substrate experimental geometry using ABAQUS 6.14 (Dassault Systemes Americas Corp., Waltham, MA). The elastic modulus of the synthetic tissue material was varied between 10 kPa and 20 kPa and the resulting simulation load-displacement output curves were compared to the corresponding experimental data. More details for the finite element model are provided in the supporting information of this document.

2.2 Correction Factor Determination

As mentioned in Section 2.1.2, the conventional JKR contact theory[2] cannot be used to interpret the indentation experiments used for adhesion characterization because the experimental contact geometry (Figure 2) is significantly different from the conventional contact geometry (Figure 1). There are two key features of the authors' specific experimental contact geometry which differ from the conventional contact geometry.

First, the layer of synthetic tissue around the rigid spherical core is not thick enough to neglect the presence of the rigid core, suggesting that there is a finite thickness restriction. Kenneth Shull has previously developed correction factors which account for the finite thickness of a compliant substrate using finite element analysis and comparing simulation results to various experimentalists' results.[6,38] For Hertz-type contact, Shull defines the finite thickness correction factors for load (f_P), displacement (f_δ) and compliance (f_C) in a general form using Equations 1-3.

$$f_P\left(\frac{a}{h}\right) = \frac{P'}{P_H} = \left(1 + \beta\left(\frac{a}{h}\right)^3\right) \tag{1}$$

$$f_\delta\left(\frac{a}{h}\right) = \frac{\delta'}{\delta_H} = \left(0.4 + 0.6exp\left(\frac{-1.8a}{h}\right)\right) \tag{2}$$

$$\frac{1}{f_C\left(\frac{a}{h}\right)} = \frac{C_o}{C} = 1 + \left(\frac{0.75}{\left(\left(\frac{a}{h}\right) + \left(\frac{a}{h}\right)^3\right)} + \frac{2.8 + (1 - 2\nu)}{\left(\frac{a}{h}\right)}\right)^{-1} \tag{3}$$

Here, a represents the contact radius, h represents the substrate thickness, and P_H, δ_H and C_o are the Hertz form of load, displacement and compliance, respectively, as defined in Equations 4-6. P', δ' and C are the measured load, displacement and compliance, respectively.

$$P_H = \frac{4E^*a^3}{3R} \tag{4}$$

$$\delta_H = \frac{a^2}{R} \tag{5}$$

$$C_o = \frac{1}{2E^*a} \tag{6}$$

E^* is the effective modulus as defined below.

$$E^* = \frac{E}{1-\nu^2} \tag{7}$$

Once the Hertz-type contact correction factors were defined, Shull used them to determine finite thickness correction factors for JKR-type contact. This was done using the general equations for energy release rate ($\mathcal{G}$). The energy release rate describes the energetic driving force for interfacial attraction or separation and the consequent increase or decrease in contact area, respectively. During the attraction regime, once the energy release rate reaches a critical value ($\mathcal{G}_{c,adh}$), the two surfaces will "jump" into contact and the contact area will grow such that the system reaches an equilibrium. Similarly, upon retraction, once the energy release rate reaches a new critical value ($\mathcal{G}_{c,sep}$), the interfacial crack between the two contacting surfaces will propagate and the two surfaces will separate. The critical energy release rate for both the attraction and separation regimes is equal to what is termed the work of adhesion (w_{adh}) and work of separation (w_{sep}), respectively. Load (P') and displacement (δ') are related through compliance (C), thus the energy release rate can be written in terms of load (Equation 8) or displacement (Equation 9).

$$\mathcal{G}_P = -\frac{(P'-P)^2}{4\pi a}\frac{\partial C}{\partial a} \tag{8}$$

$$\mathcal{G}_\delta = -\frac{(\delta'-\delta)^2}{4\pi a C^2}\frac{\partial C}{\partial a} \tag{9}$$

In these equations, primed variables represent Hertz forms of load and displacement while un-primed variables represent JKR forms of load and displacement. Shull defined the corresponding finite thickness correction factors with respect to load ($f_{\mathcal{G}_P}$) and displacement ($f_{\mathcal{G}_\delta}$). When the contacting substrates are assumed incompressible (i.e. $\nu = 0.5$), Shull's finite thickness correction factors are written as:

$$\mathcal{G}_P = \frac{(P' - P)^2}{8\pi E^* a^3} f_{\mathcal{G}_P}, \quad f_{\mathcal{G}_P} = \left(\frac{0.56 + 1.5\left(\frac{a}{h}\right) + 3\left(\frac{a}{h}\right)^3}{\left(0.75 + \left(\frac{a}{h}\right) + \left(\frac{a}{h}\right)^3\right)^2} \right) \tag{10}$$

$$\mathcal{G}_\delta = \frac{E^*(\delta' - \delta)^2}{2\pi a} f_{\mathcal{G}_\delta}, \quad f_{\mathcal{G}_\delta} = \left(1 + 2.67\left(\frac{a}{h}\right) + 5.33\left(\frac{a}{h}\right)^3\right) \tag{11}$$

The second feature of the authors' experimental contact geometries (Figure 2) which differs from the conventional contact geometries (Figure 1), is the curvature of the synthetic tissue substrate around the rigid spherical core. This curvature may result in different load, displacement and compliance measurements than those measured from a flat synthetic tissue substrate. Therefore, the authors performed additional finite element model simulations to quantify this influence while neglecting adhesion effects. The resultant load, displacement and compliance data from the simulations was used to determine correction factors for both of the experimental contact geometries shown in Figure 2. The same mathematical procedures used by Shull - and as described previously - were used to find the new correction factors. These correction factors will be referred to as, "modified-Shull" correction factors from this point on.

2.3 Adhesion Characterization

Once material properties were characterized and the new experimental contact geometry validated, experimental adhesion characterization tests were executed. Two experimental cases were tested: Case 1 - synthetic tissue probe on smooth PDMS and Case 2 - synthetic tissue probe on micro-patterned PDMS. Case 1 was used to validate the modified-Shull correction factors and as a control for comparison against Case 2.

3 Results and Discussion

The results and related discussion for the material characterization, correction factor determination and adhesion characterization are presented here.

3.1 Material Property Characterization

3.1.1 PDMS Modulus

Three experimental indentation tests were performed. Tests were displacement controlled, thus a mean of the three load measurements at each displacement point was calculated to construct a mean data set. Standard deviations of load measurements were calculated and are shown as vertical error-bars in Figure 3a. Because no adhesive forces were observed during the down-stroke test phase, Hertz contact theory with Shull's finite thickness correction factors[6] - to account for the finite thickness of the PDMS substrate ($h_{PDMS} = 1\,\mathrm{mm}$) - were used to calculate theoretical force-displacement curves. The elastic modulus of the PDMS substrate was varied in the theoretical calculations and resultant curves were compared to the mean experimental data set. The authors found that a PDMS substrate elastic modulus equal to 2.9 MPa minimized the root-mean-square-error (RMSE) between the experimental and theoretical data (Figure 3a). In this case the magnitude of the RSME is 0.05 %. This result is consistent with other PDMS elastic modulus measurements reported in the literature.[9,39]

3.1.2 Synthetic Tissue Modulus

As mentioned in Section 2.1.2, elastic modulus values ranging 10 kPa to 20 kPa were used to describe the synthetic tissue material in the finite element model. Load-displacement data was extracted from the simulations and compared to the experimental data to determine the synthetic tissue modulus which best reflected experimental results. RMSE values were calculated for each simulation-experiment combination. The minimized RMSE value

($RMSE = 0.0023\,\%$) corresponded to the simulation which defined the elastic modulus of the synthetic tissue as 15 kPa. The load-displacement curves for this particular simulation are shown in Figure 3b and are compared to the experimental data. Again, the experimental data is a mean data set calculated from three experimental trials. The the mean load was calculated at each displacement point as well as standard deviations of the mean, represented as vertical error-bars. As can be observed in Figure 3b, the simulation data lies within the error-bars of the experimental data, thus indicating that the synthetic tissue modulus is well approximated by 15 kPa.

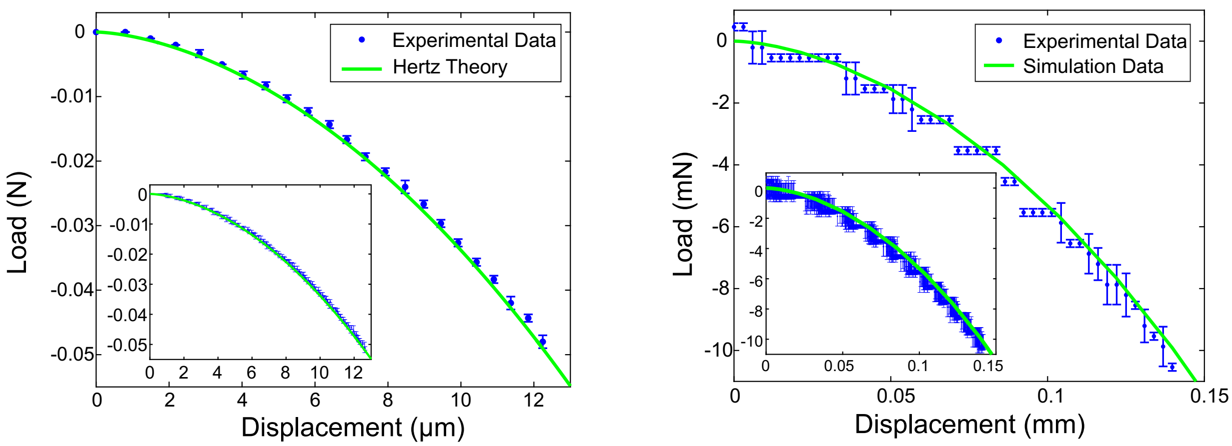

(a) (b)

Figure 3: The results of the material characterization studies for the PDMS substrate and soft synthetic tissue are presented in Figure 3a and 3b, respectively. For clarity, seven data points and twenty nine data points have been suppressed between each visible data point in Figures 3a and 3b, respectively. The inset plots in 3a and 3b show all of the experimental data and error-bars with out suppression. In Figure 3b, the apparent steps in the data are due to the load cell resolution.

3.2 Correction Factor Determination

Modified-Shull correction factors for load, displacement and compliance were determined for both experimental contact geometries: Case 1 - synthetic tissue probe on smooth PDMS (Figure 2a) and Case 2 - synthetic tissue probe on micro-patterned PDMS (Figure 2b). As mentioned in Section 2.2, the resultant load-displacement data from the finite element models, developed for each experimental geometry, was used to help determine these correction factors. The correction factors were determined by fitting a curve to the calculated results of Equations 1-3, where the measured load and displacement were equal to the load and displacement measurements from the finite element model simulations. The function forms used for Shull's finite thickness correction factors were preserved in this curve fitting process. Additionally, the curve fit was constrained to pass through the point $(0, 1)$ to ensure when finite thickness is no longer a necessary assumption (i.e. $\frac{a}{h} \to 0$), the conventional Hertz forms of load, displacement and compliance are recovered.

The calculated Hertz-type correction factor data (blue markers) for load, displacement and compliance are shown in Figures 4a-4c for the smooth PDMS experimental geometry case and in Figures 4d-4f for the micro-patterned PDMS experimental case. The constraint point is highlighted by the green "x" and the black curve represents the fitted correction factor curve. The initial 1 to 6 calculated data points were excluded from the fitting procedure. The contact radii which correspond to these initial points result in very small Hertz load and displacement values. Therefore, the errors in the first six data points are magnified and likely due to numerical artifacts. The authors recognize that choosing the points to exclude is subjective; however, it was necessary to obtain accurate functions for the modified-Shull correction factors. For comparison, Shull's finite thickness correction factors (red curves) are also shown in Figure 4. It is clear that for each experimental geometry case, Shull's finite thickness correction factors (red curves) are not sufficient to predict the response from the finite element models (blue markers).

The authors observed an interesting behavior in the calculated compliance correction factor data for the micro-patterned PDMS substrate case (Figure 4f). For values of $\frac{a}{h} <$ 0.25, the calculated compliance correction factor drops below unity, whereas the calculated compliance correction factor for the smooth PDMS substrate is greater than unity for all values of $\frac{a}{h}$ greater than zero. This behavior indicates that the compliance measured during the small contact radius region ($\frac{a}{h} < 0.25$) of the synthetic tissue probe compressing into the

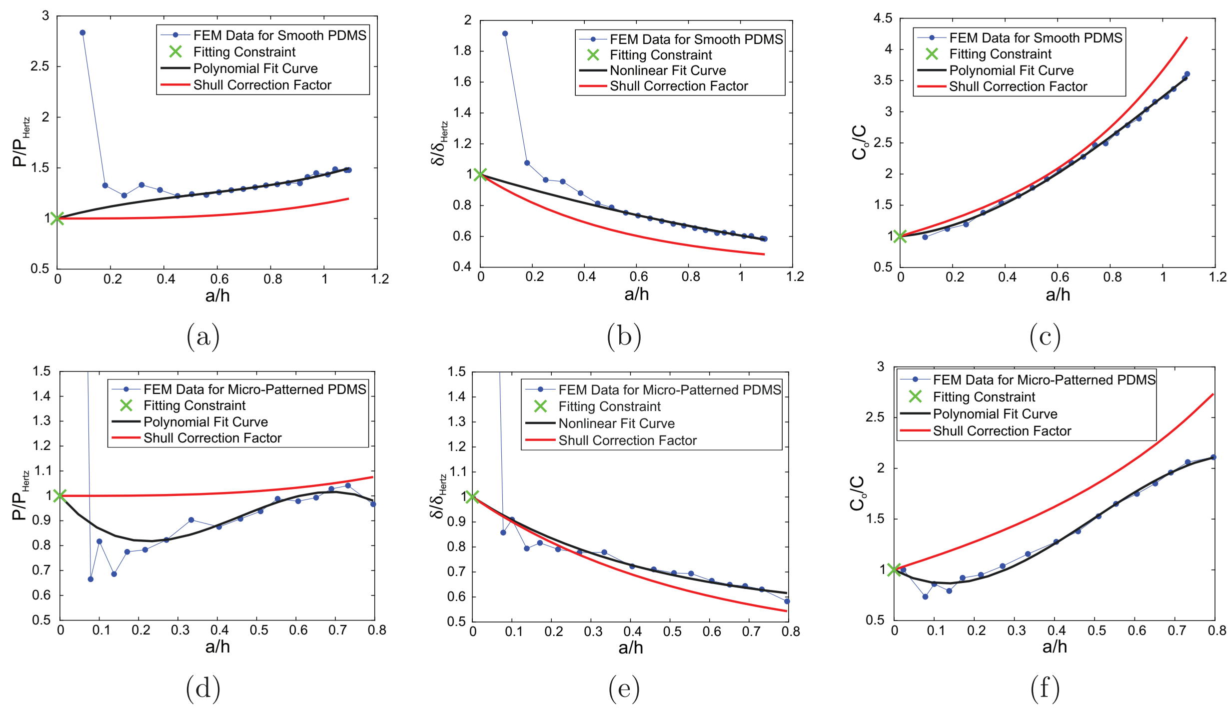

Figure 4: The calculated correction factor data (blue markers) from the finite element model simulations for the smooth PDMS (4a-4c) and micro-patterned PDMS (4d-4f) experimental geometries are shown as a function of $\frac{a}{h}$. These results are compared to the finite thickness correction factors defined by Shull (red curves). A polynomial or non-linear curve (black curve) was fit to the finite element data such that a new correction factor function was identified for each variable. The fitted functions were constrained to pass through the point $(0, 1)$.

micro-patterned PDMS substrate is greater than the Hertzian form of compliance (Equation 6). In other words, this indicates that the synthetic tissue material deforms more at small contact radii than it does at larger contact radii with respect to the same loading profiles. The authors suspect that the micro-pattern geometry (both pillar diameter and spacing) is a factor in this unique behavior. The exact characteristics of the micro-pattern structure which contribute to the increased material compliance are not studied in this work as they are outside the scope of work. However, the authors suspect that the micro-pattern geometry allows the synthetic tissue substrate to penetrate into the pillar spacing, thus increasing the system compliance. The authors plan to further investigate the micro-pattern geometry and determine how characteristics such as pillar spacing, pillar diameter and pillar height affect the contact response.

Table 1 lists the modified-Shull correction factors for load, displacement and compliance determined for both experimental cases.

Table 1: Modified-Shull correction factors for load (f_P), displacement (f_δ) and compliance $\left(\frac{1}{f_C}\right)$ for both experimental contact geometries, synthetic tissue probe on smooth PDMS and micro-patterned PDMS.

Correction Factor		**Smooth PDMS**	**Micro-Patterned PDMS**
Load:	$p_3 =$	0.49	−3.9
$f_P\left(\frac{a}{h}\right) = p_3\left(\frac{a}{h}\right)^3 + p_2\left(\frac{a}{h}\right)^2 + p_1\left(\frac{a}{h}\right) + p_0$	$p_2 =$	−0.80	5.3
	$p_1 =$	0.74	−1.8
	$p_0 =$	1.0	1.0
Displacement:	$d_2 =$	0.05	0.53
$f_\delta\left(\frac{a}{h}\right) = d_2 + d_1 \exp\left(d_0 \frac{a}{h}\right)$	$d_1 =$	0.95	0.47
	$d_0 =$	−0.54	−2.1
Compliance:	$c_3 =$	−0.74	−6.4
$\frac{1}{f_C\left(\frac{a}{h}\right)} = c_3\left(\frac{a}{h}\right)^3 + c_2,\left(\frac{a}{h}\right)^2 + c_1\left(\frac{a}{h}\right) + c_0$	$c_2 =$	2.6	9.5
	$c_1 =$	0.42	−2.1
	$c_0 =$	1.0	1.0

From the results of the experimental tests, as will be described in detail in Section 3.3, the authors observed a clear adhesion response (tensile forces upon the approach of the synthetic tissue probe) in the down-stroke test phase for the synthetic tissue probe contacting the smooth PDMS substrate (Figure 6). However, the authors did not observe a measureable adhesive response for the synthetic tissue probe contacting the micro-patterned PDMS substrate (Figure 8). Therefore, correction factors for the energy release rate ($\mathcal{G}$) were only determined for the synthetic tissue probe contacting the smooth PDMS substrate case (Table 2).

Table 2: Modified-Shull correction factors for energy release rate in terms of load ($\mathcal{G}_P$) and displacement ($\mathcal{G}_\delta$) for the synthetic tissue probe contacting the smooth PDMS substrate. The coefficients ($c_3,\ c_2,\ c_1,\ c_0$) are defined in Table 1.

Load Form	Displacement Form
$\mathcal{G}_P = \frac{(P'-P)^2}{8\pi E^* a^3} f_{GP}$	$\mathcal{G}_\delta = \frac{E^*(\delta'-\delta)^2}{2\pi a} f_{G\delta}$
$f_{GP} = \frac{4c_3\left(\frac{a}{h}\right)^3+3c_2\left(\frac{a}{h}\right)^2+2c_1\left(\frac{a}{h}\right)+c_0}{\left(c_3\left(\frac{a}{h}\right)^3+c_2\left(\frac{a}{h}\right)^2+c_1\left(\frac{a}{h}\right)+c_0\right)^2}$	$f_{G\delta} = 4c_3\left(\frac{a}{h}\right)^3 + 3c_2\left(\frac{a}{h}\right)^2 + 2c_1\left(\frac{a}{h}\right) + c_0$

The energy release rate during the down-stroke (approach) test phase was calculated in terms of load ($\mathcal{G}_P$) and displacement ($\mathcal{G}_\delta$), as defined by Equations 8 and 9, using the correction factors for load displacement and compliance as defined in Table 1. Both forms of the energy release rate were calculated and compared against contact radius as shown in the bottom panel of Figure 5. The energy release rate was also calculated using Shull's finite thickness correction factors and is shown in the top panel of Figure 5 for comparison.

As described in Section 2.2, the work of adhesion (w_{adh}) and work of separation (w_{sep}) of a contact interface are equal to the respective critical value of the energy release rate ($\mathcal{G}_c$). The critical value of the energy release rate can be extracted when comparing energy release rate to contact radius and is defined by the plateau value of the energy release rate. In theory, the two energy release rate equations (Equations 8 and 9) are equivalent, since compliance is a function of load and displacement. Thus, the work of adhesion (w_{adh}) or work of separation (w_{sep}) extracted from both energy release rate equations are equivalent.

The authors chose to calculate the work of adhesion (w_{adh}) for the contact between the

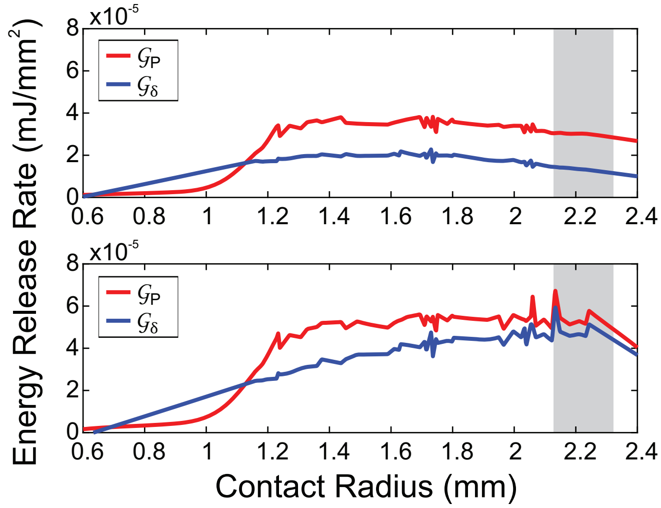

Figure 5: This figure plots the energy release rate vs. contact radius during the downstroke (approach) test phase calculated from Equations 8 ($\mathcal{G}_P$) and 9 ($\mathcal{G}_\delta$) using Shull's finite thickness correction factors (top panel) and the modified-Shull correction factors (bottom panel). For clarity, the raw data was fit with a smoothing spline curve. The smoothing parameters for each panel are equal to 0.999 and 0.985 for the energy release rate with respect to load (red curves) and displacement (blue curves), respectively. The highlighted region of each curve depicts the section of data used to extract the work of adhesion (w_{adh}).

smooth PDMS and synthetic tissue substrates from the final 300 data points of the energy release rate vs. contact radius curves (Figure 5). Clearly, the work of adhesion (w_{adh}) calculated from the energy release rate curves defined using Shull's finite thickness correction factors (Figure 5 top panel) are not equivalent, differing by a factor of approximately three (approximately 300 % error). Conversely, the work of adhesion (w_{adh}) calculated from the energy release rate curves defined using the modified-Shull correction factors (Figure 5 bottom panel) have an approximate error of 10 %. This is a validation that the modified-Shull correction factors, developed through the finite element model results, can be used to more accurately predict the experimental load-displacement behavior of the authors' specific experimental geometry. The authors attribute the small error between the two work of adhesion calculations using the modified-Shull correction factors to the manual synchronization between the load-displacement data from the MTS machine and the contact radius data from the high speed camera. The synchronization was done by analyzing the derivative of the load-displacement data to identify the point of initial contact. Because the experimental tests were displacement controlled, the authors chose to report the work of adhesion (w_{adh}) for the synthetic tissue probe contacting the smooth PDMS from the energy release rate from the value calculated with respect to displacement (blue curve). Thus, the work of adhesion (w_{adh}) for this experimental case is equal to $4.7 \times 10^{-5}\,\mathrm{mJ/mm^2}$ ($0.047\,\mathrm{J/m^2}$).

3.3 Adhesion Characterization

The overarching goal of this work is to determine if the adhesion response at the contact interface of a synthetic tissue and PDMS substrate is affected by a micro-pattern on the PDMS substrate. Two experimental tests were executed to study this interaction: Case 1 - synthetic tissue probe contacting a smooth PDMS substrate and Case 2 - synthetic tissue probe contacting a micro-patterned PDMS substrate. Experimental data was compared to theoretical predictions using the modified-Shull correction factors as well as Shull's finite thickness correction factors in order to directly extract a work of adhesion (w_{adh}) for each experimental case. The work of separation (w_{sep}) for each experimental case was estimated using the experimental data and correction factors developed from the approach test phase.

The authors would like to acknowledge that the work of adhesion (w_{adh}) and work of separation (w_{sep}) values presented in this work are rate dependent and should only be used directly for applications utilizing similar approach and retraction rates. In general, there are two sources of rate dependence which can affect adhesion: (1) rate dependent surface processes during approach and retraction testing phases and (2) viscoelasticity of the compliant substrate. For the work presented here, the authors claim that the viscoelasticity of the synthetic tissue substrate is not significant enough to contribute to the rate dependence of the work of adhesion (w_{adh}) or work of separation (w_{sep}) because the instantaneous and long-term indentation loads for the material only vary by approximately 4 % over the course of 300 s (see supporting information for more details).

3.3.1 Extracting the Work of Adhesion

3.3.1.1 Case 1: Synthetic Tissue Probe Contacting a Smooth PDMS Substrate

The experimental contact geometry for this case is the synthetic tissue probe contacting a smooth PDMS substrate (Figure 2a). Three experimental trials were executed and a mean load-displacement curve was generated. The experimental data for the down-stroke (approach) test phase is shown in Figure 6 where the error-bars indicate the standard deviation of the calculated mean load values. This experimental geometry was tested to serve as a control case as well as a validation case for the modified-Shull correction factors determined in Section 3.2.

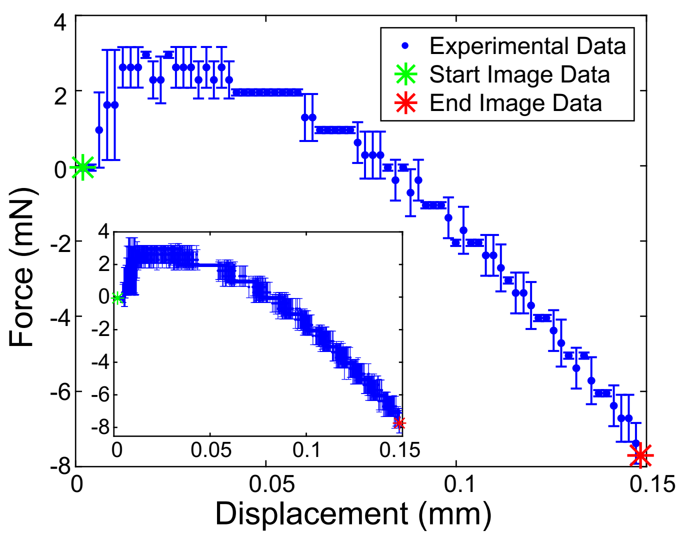

Figure 6: This plot shows the mean load-displacement data for the down-stroke (approach) test phase on smooth PDMS, where the error bars indicate the standard deviation of the mean load values. For clarity, 19 data points have been suppressed between each visible data point shown in this figure. The inset plot shows all experimental data and error-bars with out suppression. Compression forces are represented as negative forces and tensile forces are positive. The green asterisk indicates the point just before initial contact occurs while the red asterisk indicates the location of the final image frame collected. The apparent steps in the data are due to the load cell resolution.

Using the work of adhesion (w_{adh}) and modified-Shull correction factors for the smooth PDMS experimental geometry case, determined in Section 3.2, theoretical predictions for load and displacement were calculated using the JKR formulations of load (P_{JKR}) and displacement (δ_{JKR}) as defined in Equations 12 and 13, respectively.

$$P_{JKR} = P_H f_P \left(\frac{a}{h}\right) - 2\sqrt{2\pi E^* w a^3} \tag{12}$$

$$\delta_{JKR} = \delta_H f_\delta \left(\frac{a}{h}\right) - \sqrt{\frac{2\pi a w}{E^*}} \tag{13}$$

Figures 7a-7c compare the experimental (blue markers and error bars) and theoretical (red and black curves) load vs. contact radius, displacement vs. contact radius and load vs. displacement curves, respectively. In these figures, the theoretical predictions using the modified-Shull correction factors are depicted by the black curves while the theoretical predictions using Shull's finite thickness correction factors are depicted by the red curves. The authors observe that the modified-Shull correction factors predict the experimental response more accurately than Shull's finite thickness correction factors, thus validating the modified-Shull correction factors and extracted work of adhesion (w_{adh}).

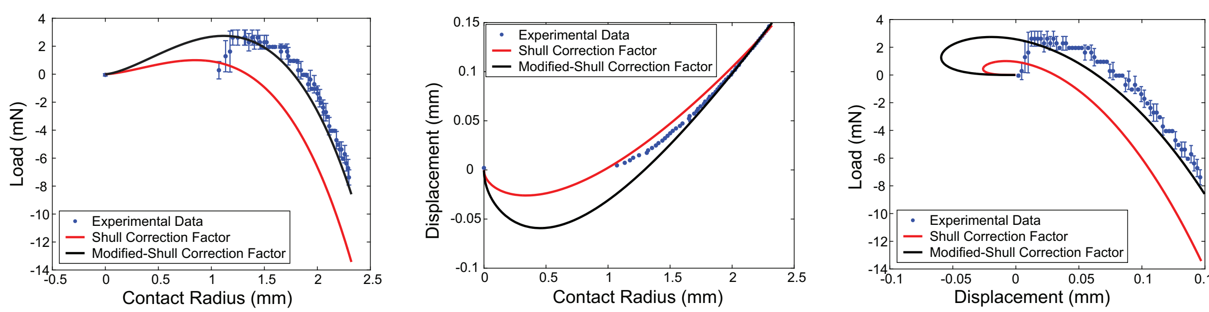

(a) (b) (c)

Figure 7: The experimental load, displacement and contact radius measurements (blue) are compared to the theoretical JKR curves using the modified-Shull correction factors (black) and Shull's finite thickness correction factors (red). For clarity, 24 data points have been suppressed between each visible data point shown in this figure. The apparent steps in the data are due to the load cell resolution.

3.3.1.2 Case 2: Synthetic Tissue Probe Contacting a Micro-Patterned PDMS Substrate

The experimental contact geometry for this case is the synthetic tissue probe contacting a micro-patterned PDMS substrate (Figure 2b). Three experimental trials were executed and a mean load-displacement curve was generated. The experimental data for the down-stroke (approach) test phase is shown in Figure 8, where the error-bars indicate the standard deviation of the mean load.

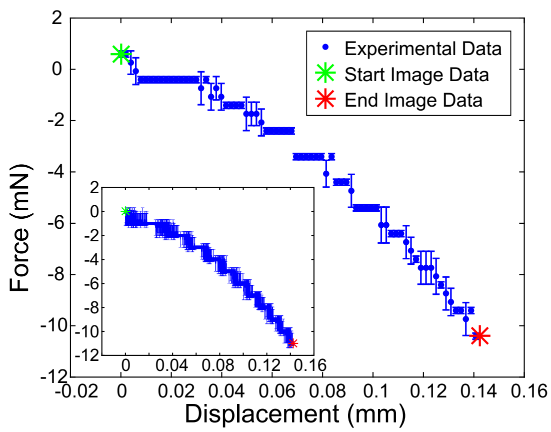

Figure 8: This plot shows the mean load-displacement data for the down-stroke (approach) test phase on micro-patterned PDMS, where the error bars indicate the standard deviation of the mean values. For clarity, 19 data points have been suppressed between each visible data point shown in this figure. The inset plot shows all experimental data and error-bars with out suppression. Compression forces are represented as negative forces and tensile forces are positive. The green asterisk indicates the point just before initial contact occurs while the red asterisk indicates the location of the final image frame collected. The apparent steps in the data are due to the load cell resolution.

As mentioned previously, the authors observed no measurable adhesive forces during the down-stroke (approach) test phase for this experimental contact geometry. This is most likely due to the discontinuity of true contact as a result of the micro-patterned cylindrical pillar geometry. Not only is the total surface energy of the micro-patterned PDMS less than that of the smooth PDMS, but the fact that the available contact sites are separated, likely decreases the attraction between the two surfaces. Therefore, the authors used the Hertz form of the contact equations (Equations 4 and 5) along with the modified-Shull correction factors for the micro-patterned PDMS experimental geometry, determined in Section 3.2, to calculate theoretical predictions for load and displacement. Shull's finite thickness correction factors were also used to calculate theoretical predictions and compared to both the experimental and modified-Shull theoretical results.

Figures 9a-9c compare the experimental (blue markers and error bars) and theoretical (red and black curves) load vs. contact radius, displacement vs. contact radius and load vs. displacement curves, respectively. In these figures, the theoretical predictions using the modified-Shull correction factors are depicted by the black curves while the theoretical predictions using Shull's finite thickness correction factors are depicted by the red curves. When the contact is described only by load and displacement (Figure 9c), the theoretical curve calculated from the modified-Shull correction factors predict the experimental data more accurately than the theoretical curve calculated using Shull's finite thickness correction factors. However, when the contact radius measurements are included (Figures 9a and 9b), the error between the modified-Shull correction factor theoretical curves and the experimental data is greater, especially at large contact radius values. The authors attribute the error observed between the modified-Shull theoretical curves and the experimental curves in Figures 9a and 9b to the fact that the contact radius was manually measured in the finite element model. In the finite element simulation, only the tops of the pillars were actually in contact with the synthetic tissue substrate. ABAQUS calculates a contact radius from the actual contact area rather than an effective contact area expanding the entire region of contact. Therefore, contact radius measurements from the simulation were much less than the experimentally observed contact radii. As a result, the authors chose to estimate the contact radius manually from the finite element model simulation results. Three node points along the contact periphery were selected and distances were calculated from a common central point. The mean distance was calculated and this was done at each time iteration of the simulation. The authors believe the uncertainty in the manual contact radius measurements contribute to the errors observed between the theoretical curves when contact radius measurements were used (Figures 9a and 9b). The authors recognize this as a limitation of the finite element model.

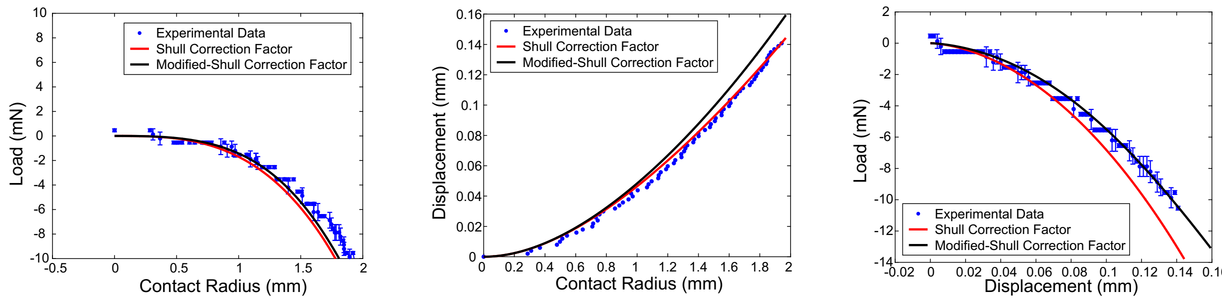

(a) (b) (c)

Figure 9: The experimental load, displacement and contact radius measurements (blue) are compared to the theoretical JKR curves using the modified-Shull correction factors (black) and Shull's finite thickness correction factors (red). For clarity, 19 data points have been suppressed between each visible data point shown in this figure. The apparent steps in the data are due to the load cell resolution.

Although no measureable tensile forces were observed during the down-stroke (approach) test phase for the micro-patterned PDMS experimental geometry, the authors wanted to provide an upper limit for what the work of adhesion (w_{adh}) for this case may be. By using the JKR formulation of the contact response (Equations 12 and 13) and the same modified-Shull correction factors, the authors varied the work of adhesion (w_{adh}) variable and compared the resulting theoretical curves to the experimental load-displacement data. Figure 10 illustrates the theoretical curve using the JKR contact equations and the modified-Shull correction factors with a work of adhesion (w_{adh}) equal to 7.2×10^{-7} mJ/mm^2 (7.2×10^{-4} J/m^2). This analysis indicates that the work of adhesion (w_{adh}) for the micro-patterned PDMS experimental contact geometry is less than 7.2×10^{-7} mJ/mm^2 (7.2×10^{-4} J/m^2).

3.3.2 Estimating the Work of Separation

For the case of an RCE, it is also critical to analyze the up-stroke (retraction) test phase as an RCE tread will be coming in and out of contact with biological tissue as it moves. As observed in Figure 11, a measureable adhesion response during retraction is observed for

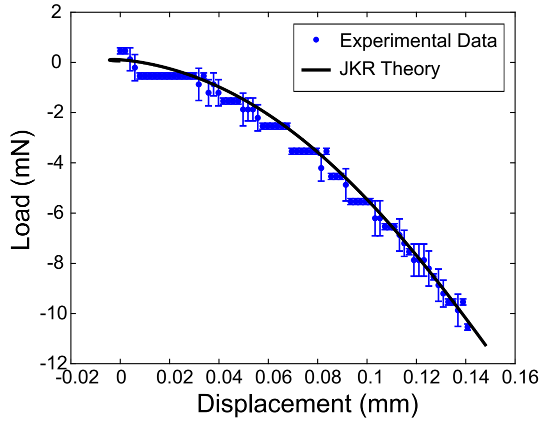

Figure 10: The experimental load and displacement is compared to the theoretical load-displacement prediction using the JKR formulation for the contact response and the modified-Shull correction factors. A work of adhesion equal to $7.2 \times 10^{-7}\,\mathrm{mJ/mm^2}$ ($7.2 \times 10^{-4}\,\mathrm{J/m^2}$) was used in the calculations, indicating that the work of adhesion for this experimental case is less than $7.2 \times 10^{-7}\,\mathrm{mJ/mm^2}$ ($7.2 \times 10^{-4}\,\mathrm{J/m^2}$). For clarity, 19 data points have been suppressed between each visible data point shown in this figure. The apparent steps in the data are due to the load cell resolution.

both experimental contact geometries. A similar data analysis procedure, as was described for the down-stroke (approach) test phase (Section 3.3.1), was done to estimate the work of separation for the smooth and micro-patterned PDMS experimental cases.

Due to camera memory and experimental limitations the contact radius was not measured during the retraction test phase (further explanation can be found in the supporting information). Thus, the authors calculated theoretical JKR adhesion curves using a range of work of separation (w_{sep}) values and a linearly spaced contact radius vector ranging from the maximum contact radius measured during the down-stroke test phase to zero. The theoretical load-displacement curves were compared to the experimental data and the estimated work of separation (w_{sep}) value was chosen based on which theoretical curve visually matched the experimental data best.

The theoretical load-displacement curves and experimental data are compared for both the smooth and micro-patterned PDMS substrates in Figure 11. In addition to the theoretical curve (magenta line) and experimental data (blue and cyan markers and error bars), a linear fit line (green line) is shown in both plots in Figure 11. This line was fit from the first

12 experimental data points in the retraction curve. The linear fit line intersects with the JKR theoretical curve at the point where the theoretical curve should begin to follow the experimental data. Upon retraction of the soft probe, the contact radius remains constant (thus producing a linear load-displacement response in the case of an elastic material) until the energy release rate reaches the critical value - work of separation (w_{sep}). Once this occurs, the contacting materials begin to separate and the contact radius decreases. Therefore, because the authors used a linearly spaced vector for the contact radius when determining the theoretical adhesion response, the experimental data is not expected to follow the entire JKR predicted curve. Only the portion of the the JKR curve which is expected to follow the experimental data is shown in Figure 11. A summary of the work of adhesion (w_{adh}) and work of separation (w_{sep}) values for both experimental contact geometries are listed in Table 3.

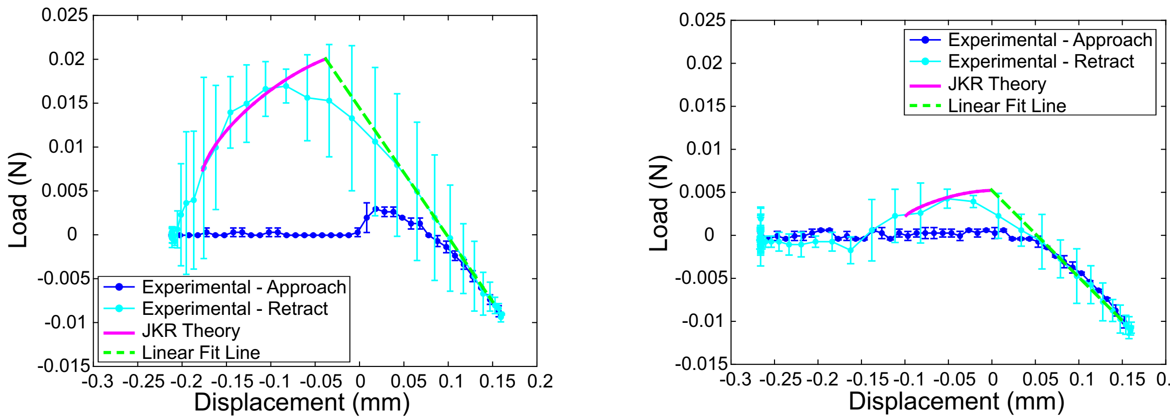

(a) (b)

Figure 11: The retraction test phase for both the smooth and micro-patterned PDMS experimental contact geometries were analyzed to extract the work of separation values. JKR theory was used to compare the theoretical response (magenta curves) to the experimental response (cyan curves). The linear fit line (green curve) intersects with the JKR theoretical curve at the point where the the theoretical curve begins to approximate the experimental data.

Table 3: Estimated work of adhesion and work of separation values for both experimental geometries.

Contact Geometry	**Work of Adhesion,** w_{adh} mJ/mm^2 (J/m^2)	**Work of Separation,** w_{sep} mJ/mm^2 (J/m^2)
Smooth	4.7×10^{-5} (0.047)	3.0×10^{-4} (0.30)
Micro-Patterned	$< 7.2 \times 10^{-7}$ (7.2×10^{-4})	8.0×10^{-5} (0.080)

4 Summary and Conclusion

In this work, the authors have presented experimental and data analysis methods for characterizing the contact and adhesive response between a soft synthetic tissue and a smooth or micro-patterned PDMS substrate. Correction factors for both experimental contact geometries (Tables 1 and 2) were defined using a finite element model and mathematical procedures presented by Shull.[6,38] Additionally, the authors observed that the specific micro-pattern geometry used for experimental testing significantly decreases the attractive response between the two substrates. For the application case of RCEs, this is an optimal response. A micro-pattern geometry which maximizes traction and minimizes adhesion allows for optimal mobility. Maximizing traction ensures the robot is advancing, rather than slipping, within the GI tract while minimizing adhesion reduces stress on the wheel driving motors and minimizes potential tissue damage.[29,35–37]

To further validate the work of adhesion (w_{adh}) and work of separation (w_{sep}) values presented in this paper, the authors have provided expected upper and lower bounds for both experimental contact geometry cases. For the case of the contact between the synthetic tissue and the smooth PDMS (Case 1), the authors would expect the work of adhesion (w_{adh}) and separation (w_{sep}) to have the following relationship:

$$w_{adh} \approx \gamma_{PDMS} + \gamma_{synthetic} - \gamma_{PDMS,synthetic} < w_{sep} \tag{14}$$

where γ refers to the surface energy of each material separately (γ_{PDMS}, $\gamma_{synthetic}$) or in contact with one another ($\gamma_{PDMS,synthetic}$). The relationship between the surface energy expression and the work of adhesion (w_{adh}) is a well known relationship derived by Dupree.[6] Further, due to the phenomenon of adhesion hysteresis[6] the work of separation should be greater than the work of adhesion. In the literature, the authors found values for the surface energy of PDMS to be approximately $23\,\text{mJ/m}^2$ and for a plasticized PVC material to be approximately $35\,\text{mJ/m}^2$.[40] No values were found for the surface energy of this specific contact pair, PDMS to plasticised PVC material. If this term is neglected, a maximum upper bound value can be calculated as the sum of the two individual surface energies. This upper bound is equal to $58\,\text{mJ/m}^2$ which indeed is greater than $45\,\text{mJ/m}^2$ and less than $300\,\text{mJ/m}^2$, the work of adhesion (w_{adh}) and work of separation (w_{sep}) reported for the contact between the synthetic tissue and smooth PDMS in this paper, respectively.

For the case of the contact between the synthetic tissue and the micro-patterned PDMS (Case 2), one may expect that the work of adhesion (w_{adh}) and work of separation (w_{sep}) could be directly scaled with the actual contact area fraction of the micro-patterned substrate. The micro-pattern geometry has cylindrical pillars which are 140 µm in diameter, 70 µm in height and equally spaced center-to-center by 256 µm. Thus, the area fraction for actual contact area (area of the tops of the pillars) can be expressed by the following:

$$f_{area} = \frac{pillar\ area\ within\ hex\ unit}{hex\ unit\ area} = \frac{3\pi r_p^2}{3a_{hex}^2} = 0.23 \tag{15}$$

where r_p is the radius of a pillar and a_{hex} is the center-to-center spacing between pillars in a hexagonal packing arrangement. Thus, one would expect the work of adhesion (w_{adh}) and work of separation (w_{sep}) for the micro-patterned cases to follow the expressions below:

$$w_{adh,pillar} \approx f_{area} w_{adh,smooth} = 10\,\text{mJ/m}^2 \tag{16}$$

$$w_{sep,pillar} \approx f_{area} w_{sep,smooth} = 70\,\text{mJ/m}^2 \tag{17}$$

These relationships assume that the actual contact area is the only factor affecting the work of adhesion (w_{adh}) or work of separation (w_{sep}). This may be a valid assumption for the case of the work of separation (w_{sep}) as the value estimated from Equation 17 ($70\,\mathrm{mJ/m^2}$) is similar to that reported by the authors from experimental testing ($80\,\mathrm{mJ/m^2}$). However, even the upper bound of the work of adhesion (w_{adh}) reported by the authors from the experimental work ($0.72\,\mathrm{mJ/m^2}$) is much less than the estimated value from Equation 16 ($10\,\mathrm{mJ/m^2}$). This suggests that the actual contact area may not be the only mechanism affecting the work of adhesion (w_{adh}) for the micro-patterned substrate. As mentioned in Section 3.3.1.2, the authors speculate that the physical separation of the contact sites on the micro-patterned PDMS substrate may also contribute to further reducing the work of adhesion (w_{adh}). Due to the presence of the micro-patterned structure, the system behaves more compliant due to the penetration of the synthetic tissue substrate between the pillars. This speculation is further supported by the interesting behavior of the compliance correction factor for the micro-patterned PDMS as mentioned in Section 3.2. Studying the specifics governing how the micro-pattern geometry affects the contact response was not within the scope of this paper. However, this work is ongoing and the authors plan to report how the pillar geometry affects the adhesion response in the future.

The results of this work are critical for further investigation of the adhesion response between a smooth compliant substrate and a stiff pillared surface, an area of research which has been explored far less than that for compliant pillars contacting a smooth, rigid surface. The experimental and data analysis procedures presented here can assist researchers and practitioners from a variety of fields and can be applied to many applications.

Acknowledgement

The authors would like to thank the National Science Foundation (NSF) for funding this work through grants CCMI 1235532 and CCMI 1636203. Additionally, Madalyn Kern is a Graduate Research Fellow through the NSF. Yuan Qi and Dr. Rong Long acknowledge start-up support from the University of Colorado at Boulder.

Supporting Information Available

This material is available free of charge via the Internet at http://pubs.acs.org/.

References

(1) Derjaguin, B. V.; Muller, V. M.; Toporov, Y. P. Effect of contact deformations on the adhesion of particles. *Journal of Colloid and interface science* **1975**, *53*, 314–326.

(2) Johnson, K. L.; Kendall, K.; Roberts, A. D. Surface Energy and the Contact of Elastic Solids. *Proceedings of the Royal Society of London. A. Mathematical and Physical Sciences* **1971**, *324*, 301–313.

(3) Fuller, K.; Tabor, D. The effect of surface roughness on the adhesion of elastic solids. *Proceedings of the Royal Society of London* **1975**, *345*, 327–342.

(4) Tabor, D. International Conference on Colloids and Surfaces: Surface forces and surface interactions. *Journal of Colloid and Interface Science* **1977**, *58*, 2–13.

(5) Barquins, M.; Maugis, D. Tackiness of Elastomers. *The Journal of Adhesion* **1981**, *13*, 53–65.

(6) Shull, K. R. Contact mechanics and the adhesion of soft solids. *Materials Science and Engineering: R: Reports* **2002**, *36*, 1–45.

(7) Glassmaker, N. J.; Jagota, A.; Hui, C.-Y.; Kim, J. Design of biomimetic fibrillar interfaces: 1. Making contact. *Journal of The Royal Society Interface* **2004**, *1*, 23–33.

(8) Hui, C.-Y.; Glassmaker, N. J.; Tang, T.; Jagota, A. Design of biomimetic fibrillar interfaces: 2. Mechanics of enhanced adhesion. *Journal of The Royal Society Interface* **2004**, *1*, 35–48.

(9) Crosby, A. J.; Hageman, M.; Duncan, A. Controlling Polymer Adhesion with "Pancakes". *Langmuir* **2005**, *21*, 11738–11743.

(10) Tang, T.; Hui, C.-Y.; Glassmaker, N. J. Can a fibrillar interface be stronger and tougher than a non-fibrillar one? *Journal of The Royal Society Interface* **2005**, *2*, 505–516.

(11) Greiner, C.; del Campo, A.; Arzt, E. Adhesion of Bioinspired Micropatterned Surfaces: Effects of Pillar Radius, Aspect Ratio, and Preload. *Langmuir* **2007**, *23*, 3495–3502.

(12) Long, R.; Hui, C.-Y.; Kim, S.; Sitti, M. Modeling the soft backing layer thickness effect on adhesion of elastic microfiber arrays. *Journal of Applied Physics* **2008**, *104*, 044301.

(13) Vajpayee, S.; Long, R.; Shen, L.; Jagota, A.; Hui, C.-Y. Effect of rate on adhesion and static friction of a film-terminated fibrillar interface. *Langmuir: the ACS journal of surfaces and colloids* **2009**, *25*, 2765–2771.

(14) Kamperman, M.; Kroner, E.; del Campo, A.; McMeeking, R. M.; Arzt, E. Functional Adhesive Surfaces with "Gecko" Effect: The Concept of Contact Splitting. *Advanced Engineering Materials* **2010**, *12*, 335–348.

(15) Vajpayee, S.; Jagota, A.; Hui, C.-Y. Adhesion of a Fibrillar Interface on Wet and Rough Surfaces. *The Journal of Adhesion* **2010**, *86*, 39–61.

(16) Shahsavan, H.; Zhao, B. Conformal Adhesion Enhancement on Biomimetic Microstructured Surfaces. *Langmuir* **2011**, *27*, 7732–7742.

(17) Autumn, K.; Liang, Y. A.; Hsieh, S. T.; Zesch, W.; Chan, W. P.; Kenny, T. W.; Fearing, R.; Full, R. J. Adhesive force of a single gecko foot-hair. *Nature* **2000**, *405*, 681–685.

(18) Autumn, K.; Sitti, M.; Liang, Y. A.; Peattie, A. M.; Hansen, W. R.; Sponberg, S.; Kenny, T. W.; Fearing, R.; Israelachvili, J. N.; Full, R. J. Evidence for van der Waals adhesion in gecko setae. *Proceedings of the National Academy of Sciences of the United States of America* **2002**, *99*, 12252–12256.

(19) Arzt, E.; Gorb, S.; Spolenak, R. From micro to nano contacts in biological attachment devices. *Proceedings of the National Academy of Sciences* **2003**, *100*, 10603–10606.

(20) Gao, H.; Wang, X.; Yao, H.; Gorb, S.; Arzt, E. Mechanics of hierarchical adhesion structures of geckos. *Mechanics of Materials* **2005**, *37*, 275–285.

(21) Shen, L.; Hui, C.-Y.; Jagota, A. A two-dimensional model for enhanced adhesion of film-terminated fibrillar interfaces by crack trapping. *Journal of Applied Physics* **2008**, *104*, 123506.

(22) Liu, J.; Hui, C.-Y.; Jagota, A. Effect of fibril arrangement on crack trapping in a film-terminated fibrillar interface. *Journal of Polymer Science Part B: Polymer Physics* **2009**, *47*, 2368–2384.

(23) Persson, B. N. J.; Tosatti, E. The effect of surface roughness on the adhesion of elastic solids. *The Journal of Chemical Physics* **2001**, *115*, 5597–5610.

(24) Martina, D.; Creton, C.; Damman, P.; Jeusette, M.; Lindner, A. Adhesion of soft viscoelastic adhesives on periodic rough surfaces. *Soft Matter* **2012**, *8*, 5350.

(25) Menga, N.; Afferrante, L.; Carbone, G. Adhesive and adhesiveless contact mechanics of elastic layers on slightly wavy rigid substrates. *International Journal of Solids and Structures* **2016**, *88–89*, 101–109.

(26) Degrandi-Contraires, É.; Beaumont, A.; Restagno, F.; Weil, R.; Poulard, C.; Léger, L. Cassie-Wenzel-like transition in patterned soft elastomer adhesive contacts. *EPL (Europhysics Letters)* **2013**, *101*, 14001.

(27) Dies, L.; Restagno, F.; Weil, R.; Léger, L.; Poulard, C. Role of adhesion between asperities in the formation of elastic solid/solid contacts. *The European Physical Journal E* **2015**, *38*, 130.

(28) Sliker, L. J.; Wang, X.; Schoen, J. A.; Rentschler, M. E. Micropatterned Treads for In Vivo Robotic Mobility. *Journal of Medical Devices* **2010**, *4*, 041006–1–041006–8.

(29) Sliker, L. J.; Kern, M. D.; Schoen, J. A.; Rentschler, M. E. Surgical evaluation of a novel tethered robotic capsule endoscope using micro-patterned treads. *Surgical Endoscopy* **2012**, *26*, 2862–2869.

(30) Cosentino, F.; Tumino, E.; Passoni, G. R.; Morandi, E.; Capria, A. Functional evaluation of the Endotics System, a new disposable self-propelled robotic colonoscope: in vitro tests and clinical trial. *The International Journal of Artificial Organs* **2009**, *32*, 517–527.

(31) Buselli, E.; Pensabene, V.; Castrataro, P.; Valdastri, P.; Menciassi, A.; Dario, P. Evaluation of friction enhancement through soft polymer micro-patterns in active capsule endoscopy. *Measurement Science & Technology* **2010**, *21*.

(32) Ciuti, G.; Valdastri, P.; Menciassi, A.; Dario, P. Robotic magnetic steering and locomotion of capsule endoscope for diagnostic and surgical endoluminal procedures. *Robotica* **2010**, *28*, 199–207.

(33) Kwon, J.; Cheung, E.; Park, S.; Sitti, M. Friction enhancement via micro-patterned wet elastomer adhesives on small intestinal surfaces. *Biomedical Materials* **2006**, *1*, 216.

(34) Sliker, L.; Rentschler, M. The Design and Characterization of a Testing Platform for Quantitative Evaluation of Tread Performance on Multiple Biological Substrates. *IEEE Transactions on Biomedical Engineering* **2012**, *59*, 2524–2530.

(35) Sliker, L. J.; Kern, M. D.; Rentschler, M. E. An Automated Traction Measurement Platform and Empirical Model for Evaluation of Rolling Micropatterned Wheels. *IEEE/ASME Transactions on Mechatronics* **2015**, *20*, 1854–1862.

(36) Terry, B. S.; Passernig, A. C.; Hill, M. L.; Schoen, J. A.; Rentschler, M. E. Small intestine mucosal adhesivity to in vivo capsule robot materials. *Journal of the Mechanical Behavior of Biomedical Materials* **2012**, *15*, 24–32.

(37) Kern, M. D.; Ortega Alcaide, J.; Rentschler, M. E. Soft material adhesion characterization for in vivo locomotion of robotic capsule endoscopes: Experimental and modeling results. *Journal of the Mechanical Behavior of Biomedical Materials* **2014**, *39*, 257–269.

(38) Shull, K. R.; Ahn, D.; Mowery, C. L. Finite-Size Corrections to the JKR Technique for Measuring Adhesion:ÃćâĆňâĂř Soft Spherical Caps Adhering to Flat, Rigid Surfaces. *Langmuir* **1997**, *13*, 1799–1804.

(39) Carrillo, F.; Gupta, S.; Balooch, M.; Marshall, S. J.; Marshall, G. W.; Pruitt, L.; Puttlitz, C. M. Nanoindentation of polydimethylsiloxane elastomers: Effect of crosslinking, work of adhesion, and fluid environment on elastic modulus. *Journal of Materials Research* **2005**, *20*, 2820–2830.

(40) Hild, F. Surface Energy of Plastics. 2009; `http://www.tstar.com/blog/bid/33845/surface-energy-of-plastics`.

Graphical TOC Entry